



King Saud University
Arabian Journal of Chemistry

www.ksu.edu.sa
www.sciencedirect.com



ORIGINAL ARTICLE

Improved magnetic properties of self-composite $\text{SrFe}_{12}\text{O}_{19}$ powder prepared by Fe_3O_4 nanoparticles



Ruoshui Liu^{a,b,c}, Di'an Wu^d, Xiang Yu^{b,c}, Ningfang Zhou^b, Dan Liu^e,
Lichen Wang^{b,g}, Zhiyi Xu^{b,c}, Huayang Gong^b, Tongyun Zhao^{b,c}, Jirong Sun^c,
Fengxia Hu^c, Baogen Shen^{a,b,c,f,g,*}

^a School of Rare Earths, University of Science and Technology of China, Hefei, Anhui 230026, China

^b Ganjiang Innovation Academy, Chinese Academy of Sciences, Ganzhou, Jiangxi 341119, China

^c Beijing National Laboratory for Condensed Matter Physics, Institute of Physics, Chinese Academy of Sciences, Beijing 100190, China

^d Department of Physics, Capital Normal University, Beijing 100048, China

^e Department of Physics, School of Artificial Intelligence, Beijing Technology and Business University, Beijing 100048, China

^f Ningbo Institute of Materials Technology & Engineering, Chinese Academy of Sciences, Ningbo, Zhejiang 315201, China

^g Innovation Center for Applied Magnetism of Zhejiang Province, Ningbo, Zhejiang 315201, China

Received 16 May 2022; accepted 21 June 2022

Available online 25 June 2022

KEYWORDS

Strontium hexaferrite;
 Fe_3O_4 nanoparticles;
Self-composite;
Magnetic properties;
Formation mechanism

Abstract Sintered polycrystalline strontium hexaferrite, which is one of the most widely used permanent magnetic materials, has been applied in many areas such as electrical and mechanical transducer devices. Improving the coercivity (H_{cJ}) of M-type strontium hexaferrite with a nominal composition $\text{SrFe}_{12}\text{O}_{19}$ (SrM) plays an essential role to adapt to many modern applications, but is limited by the process and purity of raw materials. In this work, we prepared SrM powders with different iron resources, sintering temperatures, and Fe/Sr atom ratios. It was found that using Fe_3O_4 nanoparticles with a Fe/Sr atom ratio of 12 at 1100 °C performed the self-composites with 70% nano-size and 30% micro-size, which had the best performance. The coercivity reaches 348.9 kA/m, which is improved compared to pure SrM obtained by other iron resources in the solid-state method. This process shows a unique formation mechanism and the resulting self-composite microstructure eventually causes enhancement in the properties, which provides a new way for high-performance hexaferrites.

© 2022 The Author(s). Published by Elsevier B.V. on behalf of King Saud University. This is an open access article under the CC BY-NC-ND license (<http://creativecommons.org/licenses/by-nc-nd/4.0/>).

* Corresponding author at: School of Rare Earths, University of Science and Technology of China, Hefei, Anhui 230026, China.
E-mail address: shenbg@iphy.ac.cn (B. Shen).

Peer review under responsibility of King Saud University.



Production and hosting by Elsevier

1. Introduction

Hexaferrites are considered the most suitable “gap magnets” which can be used to substitute expensive rare earth alloy-based permanent magnets (Granados-Miralles and Jenuš, 2021). This is because of their relatively large saturation magnetization (M_s) and their high coercivity (H_{cJ}) derived from high magnetocrystalline anisotropy with an easy magnetization axis along the c -direction. At the same time, hexaferrites have strong resistivity and are resistive to corrosion. Due to these unique characteristics, they have been widely applied in some permanent magnets, high-frequency devices, and high-density magnetic recording instruments (Pullar, 2012). Therefore, there are continuous research efforts, both from fundamental and applied perspectives, to improve the magnetic parameters of M-type strontium hexaferrite $\text{SrFe}_{12}\text{O}_{19}$ (SrM) via tuning the crystallite size (Vijayalakshmi and Gajbhiye, 1998), morphology (Gu et al., 2013), microstructure (Zi et al., 2008); and chemical substitution (Li et al., 2013; Zhu et al., 2020). There are many different routes to achieving this, such as the traditional ceramic method (Sánchez-De Jesús et al., 2014; Singh et al., 2017; Oh et al., 2020), the hydrothermal method (Jean et al., 2010; Katlakunta et al., 2015), the sol-gel method (Sapoletova et al., 2015; Ashiq et al., 2015); and the molten-salt method (Kim and Kim, 2006), etc. The last two decades have witnessed huge differences in magnetic properties of SrM in different researches, which can be partly attributed to the different raw materials.

Recently, there has been a trend to prepare SrM by the conventional ceramic route starting from nanoparticles with Fe as the source (Sun et al., 2018; Xia et al., 2019; Li et al., 2020). Higher magnetic properties can be obtained mainly due to changes in the purity of raw materials and the microstructure of nanocrystalline powders. Sun et al. (Sun et al., 2018) prepared pure SrM with a relatively high M_s of 76.7 emu/g from acicular goethite (α -FeOOH) nanoparticles synthesized by a surfactant (CTAB) assisted hydrothermal method. Li et al. (2020) found that hydrothermally synthesized spindle-like α -Fe₂O₃ nanoparticles were more conducive to synthesizing a well-developed plate-like barium hexaferrite which has higher M_s compared with purchased α -Fe₂O₃. It indicates that the morphology of raw material and the preparation process influence the structure and properties of the magnets. However, as the price of high M_s , the H_{cJ} of these studies were less than 200 kA/m, which was not proper to be applied as permanent magnets.

As a source of iron ions, Fe₃O₄ exhibits strong magnetism. In its inverse spinel structure, half of the Fe³⁺ ions occupy the tetrahedral A site, and the other half occupy the octahedral B site with the same amount of Fe²⁺. Due to the strong antiferromagnetic coupling between A and B sites, the net magnetic moment per molecule is contributed by Fe²⁺ (4 μ_B) at the B site. Fe₃O₄ nanoparticles have aroused great interest in catalysis (Xia et al., 2019), hyperthermia (Li et al., 2020) and targeted drug delivery (Teja and Koh, 2009), but there are few studies in the field of hexaferrite at present. By controlling the synthesis conditions, Fe₃O₄ is ferrimagnetic at room temperature with M_s up to 75 emu/g and H_{cJ} varying from 2.4 to 20 kA/m (Teja and Koh, 2009).

Fe₃O₄ nanoparticles are usually used to fabricate composites as a soft magnetic phase with the hard hexaferrite mainly in the domain of hard-soft composites to get better performance (Remya et al., 2016). Compared with the difficulty of synthesizing hard-soft composites, the nano-micron crystallite size composite, which is called self-composite, is a simple way to adjust the microstructure of magnets and then improve the magnetic properties. For the first time, Mohaideen and Joy (2012) proposed a novel concept on cobalt ferrite particles of different sizes at the nanoscale and microscale to improve magnetostriction. Anantharamaiah and Joy (2019) also prepared nanocrystalline CoFe₂O₄ and bulk CoFe_{1.9}Ga_{0.1}O₄ magnetostrictive composites, by combining the advantages of the two components. Due to the change in the microstructure of the sintered material and the strong coupling of the two magnetic domains, the magnetostrictive

performance has been improved. Inspired by the field of magnetostrictive materials, Shashanka et al. (2019) used nanocrystalline and micro-scale SrM powders with different mass ratios to prepare self-composite materials. For a self-composite of 75 w.t.% nano and 25 w.t.% micron-sized powders, a synthesized SrM sample with H_{cJ} of 244.78 kA/m had been obtained which was larger than the values for the sintered compacts from the component powders. It also suggests that the H_{cJ} of sintered SrM can be improved by making a self-composite comprising nanocrystalline and micron-sized powders.

The primary objective of this study was to obtain higher H_{cJ} without a significant decrease in M_s for the sintered SrM. Considering the aforementioned objective, SrM was prepared starting from the thermal decomposition of synthesized Fe₃O₄ nanoparticles by a simple solid-state method. The influence of the precursors' history on the phase composition evolution was also investigated. Due to the special formation mechanism during the synthesis of SrM from Fe₃O₄ nanoparticles, magnetic properties were improved by making a self-composite from nanocrystalline and micro-sized particles. This work achieved higher H_{cJ} than existing similar works, which can provide new ideas for improving the magnetic properties of strontium hexaferrite.

2. Experiments

2.1. Synthesis of Fe₃O₄ magnetic nanoparticles

Fe₃O₄ magnetic nanoparticles (NPs) with a diameter of 12 nm were synthesized by thermal decomposition in organic solutions (Wu et al., 2014). Fe (III) acetylacetonate (3 mmol, 99%, Alfa), sodium oleate (2 mmol, 90%, Sigma), oleic acid (15 mmol, 90%, Aldrich) and 20 mL benzyl ether (99%, TongGuang) were mixed and magnetically stirred under a gentle flow of Ar. Then the mixture was heated to 120 °C for 30 min. Under Ar blanket, the solution was heated up to 295 °C at a heating rate of 5 °C/min and kept at this temperature for 2 h. The solution was then cooled down to room temperature after removing the heat source. After that, 20 mL of hexane (97%, TongGuang) and 20 mL of ethanol (99.7%, TongGuang) were added to the mixture to precipitate the product. The Fe₃O₄ NPs were collected by the magnetic separation method, and the final product was dispersed in hexane for further use.

2.2. Synthesis of SrM powders

The synthesized Fe₃O₄ NPs and reagent grade powder SrCO₃ (99.9%, Innochem) were mixed with different Fe/Sr atomic ratios of 12:1, 11:1, and 10:1. Then, the 12:1 mixture was sintered at different temperatures of 500–1100 °C at intervals of 100 °C and 1250 °C with a heating rate of 5 °C/min, while the others were sintered at 1100 °C. As a comparison, purchased reagent grade Fe₃O₄ (99%, Aladdin) and SrCO₃ were mixed with a Fe/Sr atomic ratio of 12:1 and sintered under the same conditions. Finally, the structure and magnetic properties of sintered SrM powders were characterized. To distinguish the two kinds of iron sources and the different Fe/Sr atomic ratios, the four SrM specimens were labeled as NP12, NP11, NP10, and RG12.

2.3. Characterization and measurements

The phase composition of sintered specimens at different temperatures were identified by an X-ray diffractometer (XRD,

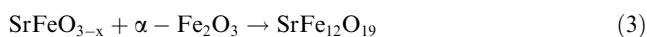
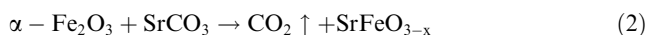
Rigaku D/Max-2400) with Cu K α radiation. The DSC and TG curves of precursor powders were measured in the N₂ atmosphere at a heating rate of 5 °C/min by thermogravimetric and differential scanning calorimeter (TG/DSC, Netzsch STA-449). The morphology of Fe₃O₄ NPs and SrM powders were detected by a transmission electron microscope (TEM, Hitachi H-7650) and a scanning electron microscope (SEM, Phenom Pro), respectively. The particle size distribution of SrM powders were examined by a laser particle size analyzer (LDPSA, Helos-Oasis). The room-temperature magnetic hysteresis loops of specimens were measured on a vibrating sample magnetometer (SQUID-VSM, Quantum Design) with the maximum external field of 7 T.

3. Results and discussion

3.1. Formation mechanism of SrM

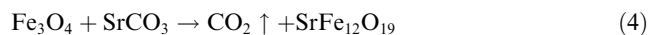
The XRD patterns of Fe₃O₄ NPs synthesized by the thermal decomposition method indicated that all the peaks had a good agreement with the standard PDF card NO.19-0629. This confirmed the existence of a single cubic phase structure, as shown in Fig. 1(a). The inset of Fig. 1(a) shows the TEM image with the histogram of the size distribution of Fe₃O₄ NPs with a relatively uniform size of 12 nm, stable morphology, and good mono-dispersity. And the Since Fe/Sr atom ratio affects the magnetic properties of SrM, specimens with different Fe/Sr ratios of 10, 11, and 12 were sintered from Fe₃O₄ NPs at 1100 °C for comparison. Fig. 1(b) shows the XRD patterns of NP12, NP11, and NP10. Only NP10 had no α -Fe₂O₃ at 1100 °C, indicating that the iron-deficient formulation was more beneficial to the formation of the pure phase. This is consistent with the conclusions of previous studies (Fu and Lin, 2005; Jean et al., 2010; Masoudpanah and Ebrahimi, 2011).

Fig. 1(c) and (d) show the phase evolution of the mixtures of SrCO₃ with reagent grade Fe₃O₄ and Fe₃O₄ NPs respectively with a Fe/Sr atom ratio of 12. The formation mechanism of SrM generated by the two kinds of Fe sources through the solid-state method was well reflected with an increase in sintering temperature. More specifically, the reagent grade Fe₃O₄ was completely oxidized to α -Fe₂O₃ (600–700 °C) at first, and then subsequently followed the general reaction process. Immediately, some of α -Fe₂O₃ reacted with SrCO₃ to form perovskite phase SrFeO_{3-x} (800 °C). Thereafter, SrFeO_{3-x} reacted with the remaining α -Fe₂O₃ to form hexagonal SrFe₁₂O₁₉ starting from 900 °C. The entire reaction process is described by the following formula:



However, when Fe₃O₄ NPs were used as an iron source, SrFeO_{3-x} and SrFe₁₂O₁₉ appeared simultaneously at 700 °C as shown in Fig. 1(d). The SrFeO_{3-x} phase still existed at 1000 °C and was not exhausted until the reaction was completed at 1100 °C. This phenomenon indicated that not only did the formation of SrFeO_{3-x} was advanced to the condition that Fe₃O₄ nanoparticles had not been completely oxidized, but also Fe₃O₄ nanoparticles directly reacted to generate

SrFe₁₂O₁₉ as described in reaction formula (4). In other words, reaction formula (4) may occur with reaction formulas (1) to (3) at the same time. This is attributed to the small size of Fe₃O₄ NPs with easy reactivity, which is key to optimizing the structure, morphology, and magnetic properties of hexagonal ferrites. A similar formation mechanism has been reported that the reaction of Fe₂O₃ and SrCO₃ after mechanical ball milling became Sr-Fe₃O₄, and then directly reacted with oxygen to form SrFe₁₂O₁₉ (Kaczmarek et al., 1998; Xu et al., 2017). The difference in the reaction process between Fe₃O₄ NPs and reagent grade Fe₃O₄ may lead to a variety of magnetic properties, whereas the intermediate phase transformation was often overlooked.



It can be seen from Fig. 1(d) that there is still unreacted α -Fe₂O₃ at 1100 °C which was eliminated at 1250 °C, the normal temperature of the solid-state method (Shen et al., 2021; Sozeri et al., 2012).

To further understand the formation mechanism of SrM, the DSC and TG curves of precursor powders were measured from room temperature to 1300 °C for comprehensive consideration with XRD results, as shown in black and blue solid lines in Fig. 2. The TG curves were differentiated to help understand the sintering reaction process of the mixture, as shown by the green dot lines in the DTG curves. As the AB segment of the TG curve in Fig. 2(a) shows, the mass of the mixture of Fe₃O₄ NPs and SrCO₃ decreased slowly with increasing temperature between room temperature and 400 °C; while the mass had no change in temperature ranging from 400 °C to 600 °C, as shown in the BC segment. The former was due to the release of gas and vapor absorbed on the surface of the mixture, and the latter implied there was no chemical reaction between Fe oxide and SrCO₃. The little hump in the BC segment represents the oxidation of Fe₃O₄ as described in the formula (1). However, when the temperature exceeded 600 °C, the TG curve dropped sharply, as shown in the CD segment. Meanwhile, there are two obvious peaks in the DTG curve between 600 °C and 750 °C, corresponding to the small endothermic peaks in the DSC curve around 667.8 °C and 708.6 °C. It means there are chemical reactions occurred. As shown in Fig. 1(c), SrFeO_{3-x} and SrFe₁₂O₁₉ were observed at 700 °C, indicating that the reaction formulas (2) to (4) took place in the CD segment. A nearly 4 % reduction of mass fraction also indicated the release of CO₂. Since the TG curve did not change as shown in the DEF segment in Fig. 2(a), no additional reaction occurred above 800 °C. That meant the main reactions were completed at 800 °C, a relatively low temperature in the solid-state method, and SrM particles mainly grew up rather than nucleated at this stage. Except for point E on the TG curve, corresponding to the endothermic peak at 1063.7 °C on the DSC curve, the reaction from the remaining SrFeO_{3-x} to SrFe₁₂O₁₉ was completed. Therefore, the pure SrM phase can be generated at 1100 °C or above, after which the particles grew up with increasing temperature.

The DSC and TG curves for the reagent agent Fe₃O₄ and SrCO₃ mixture were measured from room temperature to 1300 °C, as shown in Fig. 2(b). Dissimilar to the TG curve in Fig. 2(a), the AB segment of the TG curve in Fig. 2(b) which ranged from room temperature to 700 °C represented the evaporation of absorbed water and the oxidation of Fe₃O₄. The

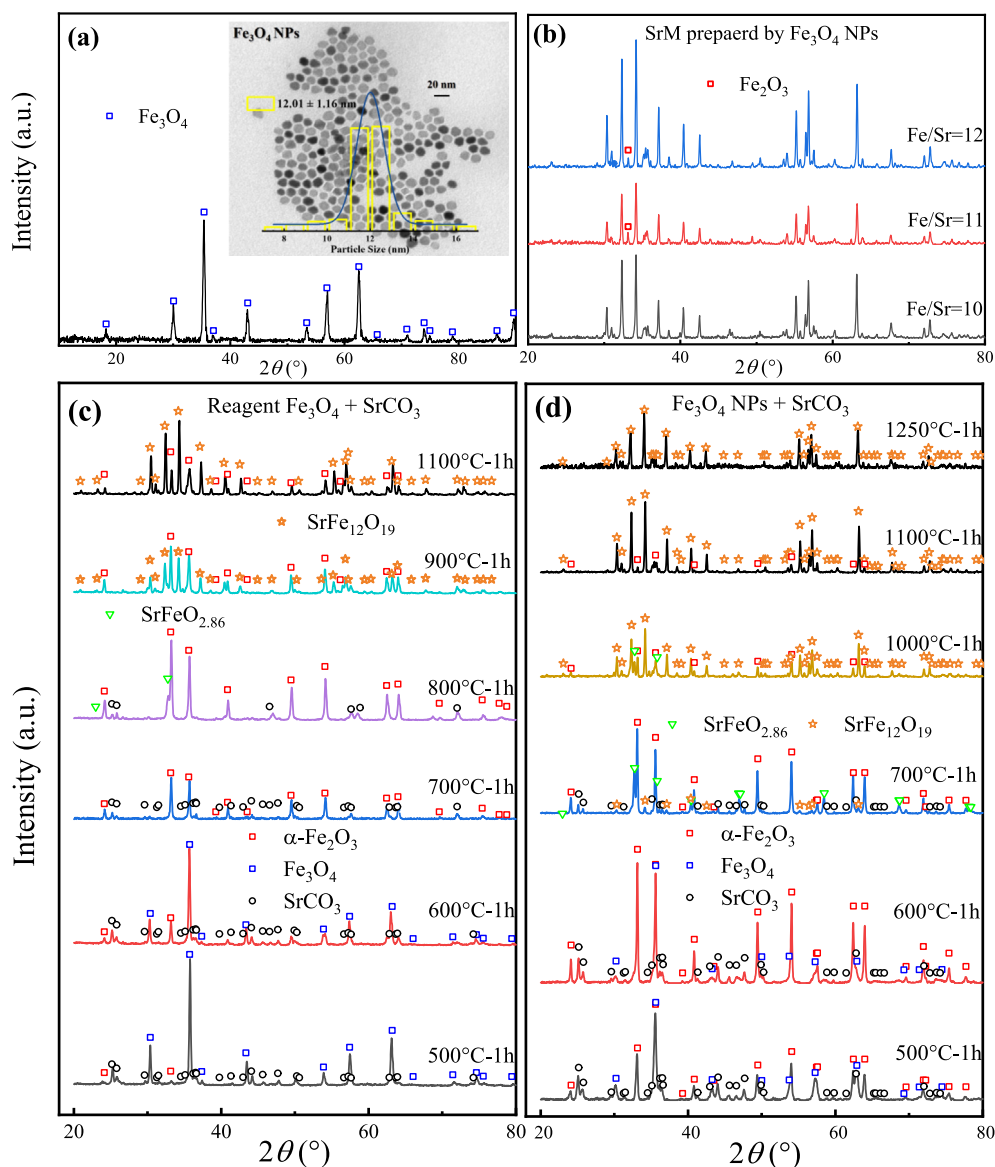


Fig. 1 XRD patterns of (a) Fe_3O_4 NPs with the inset of their TEM image and particle size distribution, (b) SrM powders prepared by Fe_3O_4 NPs with different Fe/Sr atom ratio of 10, 11 and 12 sintered at 1100 °C, (c) reagent grade Fe_3O_4 and SrCO_3 sintered at 500 to 1100 °C, (d) Fe_3O_4 NPs and SrCO_3 sintered at 500 to 1250 °C.

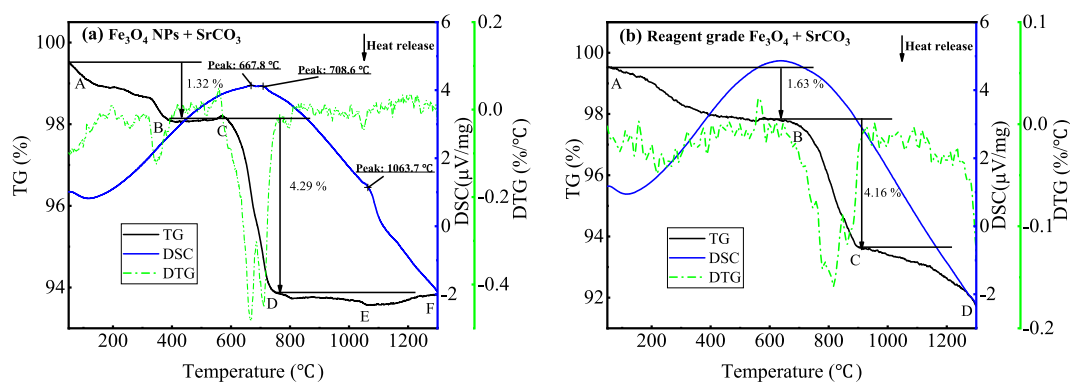


Fig. 2 DSC (blue) and TG (black) curves of (a) the mixture of Fe_3O_4 NPs and SrCO_3 and (b) the mixture of reagent grade Fe_3O_4 and SrCO_3 . The green dot lines represent differential lines of TG curves, i.e., DTG curves.

reactions did not occur until the mass fraction decreased by almost 4 % from 700 °C to 900 °C as shown in the BC segment. Corresponding to Fig. 1(d), SrFeO_{3-x} and $\text{SrFe}_{12}\text{O}_{19}$ were found in the sequence above 700 to 900 °C, as shown in formulas (2) and (3). Besides, a broad endothermic peak without humps occurred in the DSC curve. This meant no additional reactions took place in the reagent agent Fe_3O_4 mixture. With the increase in temperature, the $\alpha\text{-Fe}_2\text{O}_3$ content gradually, while the content of the $\text{SrFe}_{12}\text{O}_{19}$ turned to be much more compact such that the TG curve decreased slightly from 900 °C up to 1300 °C, as shown in the CD segment in Fig. 2(b). A similar TG curve of $\text{Sr-Fe}_3\text{O}_4$ mixture after 120 h-milled was observed by Xu et al. (2017). Based on the above discussion, it can be inferred that using Fe_3O_4 NPs as an iron resource can complete the reaction at a lower temperature and react more quickly, such that the $\text{SrFe}_{12}\text{O}_{19}$ phase can be obtained at 1100 °C. Due to the difference in particle size, reagent agent Fe_3O_4 reacts slowly at a higher temperature, and presents different reaction processes with Fe_3O_4 NPs.

3.2. Microstructure of SrM

Fig. 3(a) to (c) show the SEM images of SrM powders prepared by Fe_3O_4 NPs with a Fe/Sr atom ratio of 12, i.e., NP12, sintered at different temperatures, from which the changes of particle morphology and size during the formation process of SrM can be seen. As Fig. 3(a) shows, NP12 had an irregular shape, indicating that the SrM phase was not formed fully at 1000 °C. However, the hexagonal shape of the particles in Fig. 3(b) indicated that the SrM phase had been formed at 1100 °C. Moreover, NP12 at 1100 °C revealed a very nonuniform particle size distribution, with large particles on the micrometer scale but small on the nanometer. This phenomenon has special implications for magnetic properties, which are discussed below. Fig. 3(g) shows the energy dispersive spectrometer (EDS) measurement of NP11 at 1100 °C, which proves the homogeneity of our sample. And the atomic ratio shows a slight excess of Fe, which should be contributed to unreacted $\alpha\text{-Fe}_2\text{O}_3$. When the temperature was 1250 °C, the particle size of SrM powders increased to $\sim 3 \mu\text{m}$ as shown in Fig. 3(c), which was to the disadvantage of H_{cJ} . In conclusion, 1100 °C is the most suitable temperature for SrM preparation from Fe_3O_4 NPs by the solid-state method.

In contrast, the particle size of RG12 at 1100 °C was much more uniform and they were mostly greater than $1 \mu\text{m}$ as shown in Fig. 3(d). The difference between the microstructure of NP12 and RG12 is related to the formation mechanism described in Section 3.1, which is vividly displayed in Fig. 4. Since some of Fe_3O_4 NPs reacted directly to form SrM at low temperature (700 °C), this part of the particles underwent the process of nucleation and growth with temperature increasing, resulting in large particles. While the rest of Fe_3O_4 NPs were oxidized to $\alpha\text{-Fe}_2\text{O}_3$, then formed SrFeO_{3-x} with SrCO_3 , and finally SrM was generated. This process kept corresponding SrM particles small and led to a disparity in the particle size distribution.

Fig. 3(e) and (f) show the particle sizes of NP10 and NP11 at 1100 °C, which are both unevenly distributed. In terms of shape, the grains of NP10 were plate-like but NP11 had no regular shape. It can be concluded from Fig. 3(b), (e), and (f) that the Fe/Sr atom ratio had a significant effect on the microstructure of SrM.

As the Fe atom ratio increased (i.e., more Fe_3O_4 NPs participated in the reaction), more nanoscale SrM particles were formed. Therefore, the final particle size distribution was more disparate. Besides, the smaller the Fe/Sr ratio was, the more favorable for the formation of plate-like particles.

After the laser particle size analyzer measurement, it can be intuitively seen in Fig. 5 that the SrM powder prepared by Fe_3O_4 NPs and reagent grade Fe_3O_4 at 1100 °C had a significant difference in particle distribution. It can be seen from the The NP12, NP11 and NP10 all had “double peaks”. This meant that there were two kinds of grain composition with a large difference in particle size. Meanwhile RG12 only had a single peak distribution. Fig. 5(a) shows the particle size distribution of NP12 with smaller particle size of $0.387 \mu\text{m}$ and larger particle size of $6.158 \mu\text{m}$. These were consistent with the results observed by SEM in Fig. 3(b). It has been reported that the SrM powders in nanocrystalline and micron-size can be sintered together, which is called self-composite SrM, to achieve enhanced magnetic properties (Shashanka et al., 2019). The microstructure of NP12 shown in Fig. 3(b) is just like self-composite SrM as described, and a rough proportion can be obtained from Fig. 5(a) to be 70 % of nano and 30 % of micro.

Fig. 5(b) shows the particle size distribution of RG12 at 1100 °C. The average particle size is $1.705 \mu\text{m}$, larger than the single domain ($\sim 1 \mu\text{m}$) of SrM (Wohlfarth, 1983), which is not conducive to the high H_{cJ} . According to Fig. 5(c) and (d), changing the Fe/Sr atom ratio resulted in different proportions of small and large particles in SrM powders. For NP10, 43 % of small particles with size of $1.434 \mu\text{m}$ and 57 % of large particles with size of $16.431 \mu\text{m}$ were found. While for NP11, small particles with size of $1.302 \mu\text{m}$ accounted for 52 %, and large particles with size of $12.531 \mu\text{m}$ accounted for 48 %. Due to the special formation mechanism, the SrM powders prepared by Fe_3O_4 NPs present the self-composite of nanocrystalline and micron-sized particles, which may realize the regulation of the microstructure and enhancement of magnetic properties.

3.3. Magnetic properties of SrM

The effect of sintering temperature, types of Fe resource and Fe/Sr atom ratio on the magnetic properties for the obtained SrM are illustrated in Fig. 6(a) to (d). As can be seen from Fig. 6(a), the coercivity H_{cJ} and saturated magnetization M_{S} of NP12 sintered at 1100 °C and 1250 °C were found to be 348.9 kA/m, 97.8 kA/m and 65.8 emu/g, 69.5 emu/g, respectively. Due to the presence of $\alpha\text{-Fe}_2\text{O}_3$, the M_{S} of NP12 sintered at 1100 °C was slightly lower than 1250 °C. The SrM ferrite has high uniaxial magnetocrystalline anisotropy, while the remanence M_{r} in randomly oriented SrM samples is usually $\sim 50\%$ of the M_{S} , resulting a ratio of $M_{\text{r}}/M_{\text{S}}$ (squareness ratio, SQR) of 0.5 (Liu et al., 2019). The M_{r} and SQR of NP12 sintered at 1100 °C and 1250 °C was 0.48 and 0.37, respectively. The SQR value of NP12 at 1100 °C is close to randomly oriented samples in literature (Pullar et al., 2012), and it is obvious that high temperature is harmful to magnetic properties. Combined with the differences in microstructure of the two samples, the lower sintering temperature had a significant effect on grain size for anisotropy. In this preparation method, the high temperature of 1250 °C caused the grain size

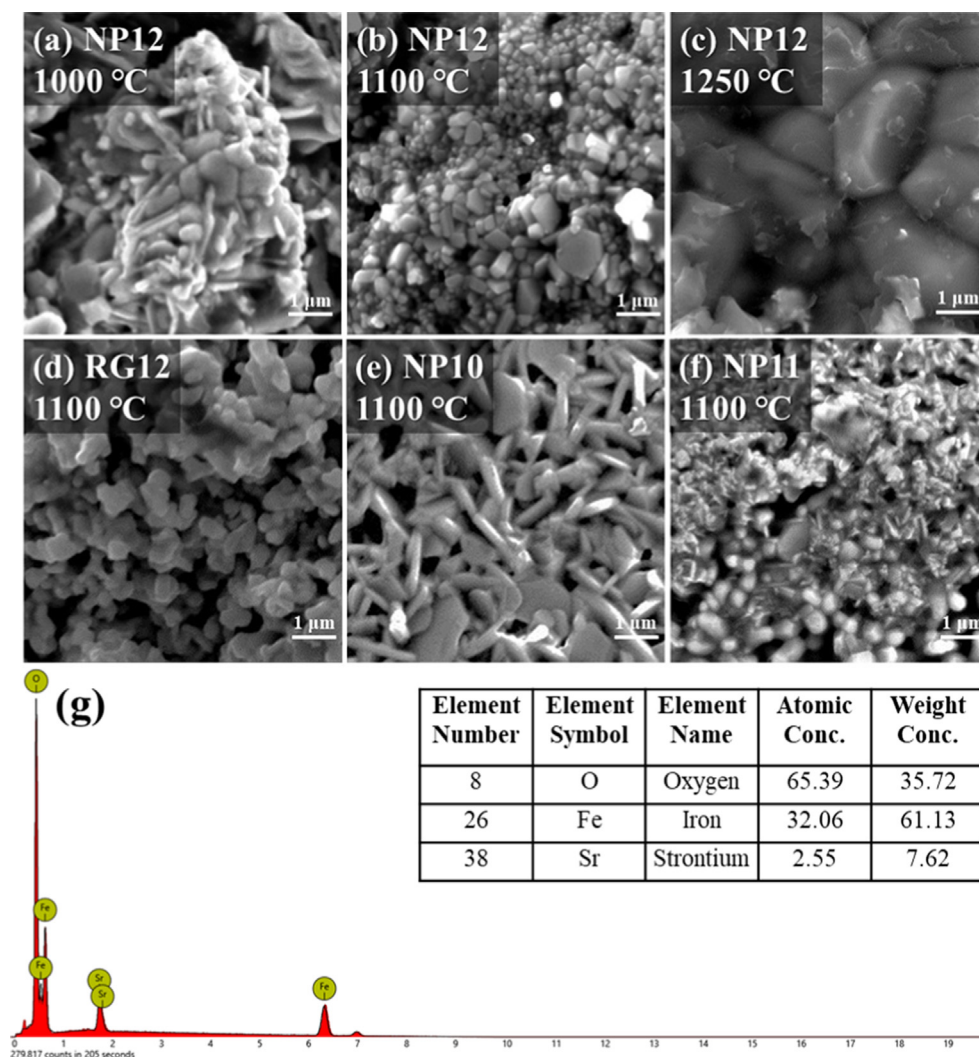


Fig. 3 SEM images (a) NP12 sintered at 1000 °C, (b) NP12 at 1100 °C, (c) NP12 at 1250 °C, (d) RG12 at 1100 °C, (e) NP10 at 1100 °C, and (f) NP11 at 1100 °C. And (g) EDS of NP12 at 1100 °C with elements identification.

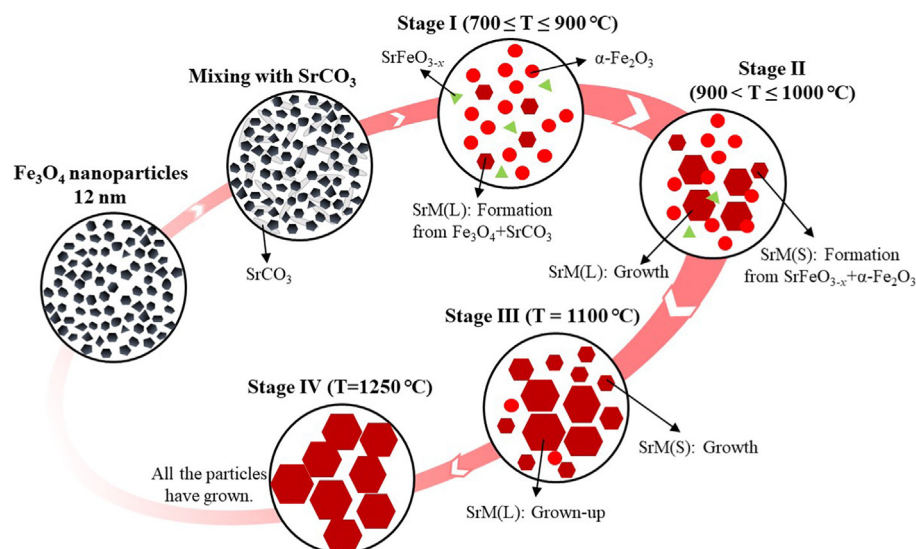


Fig. 4 The formation mechanism diagram of SrM ferrite prepared by solid-state reaction using Fe_3O_4 nanoparticles as raw material. The SrM(L) and SrM(S) represent large and small particles of $\text{SrFe}_{12}\text{O}_{19}$, respectively.

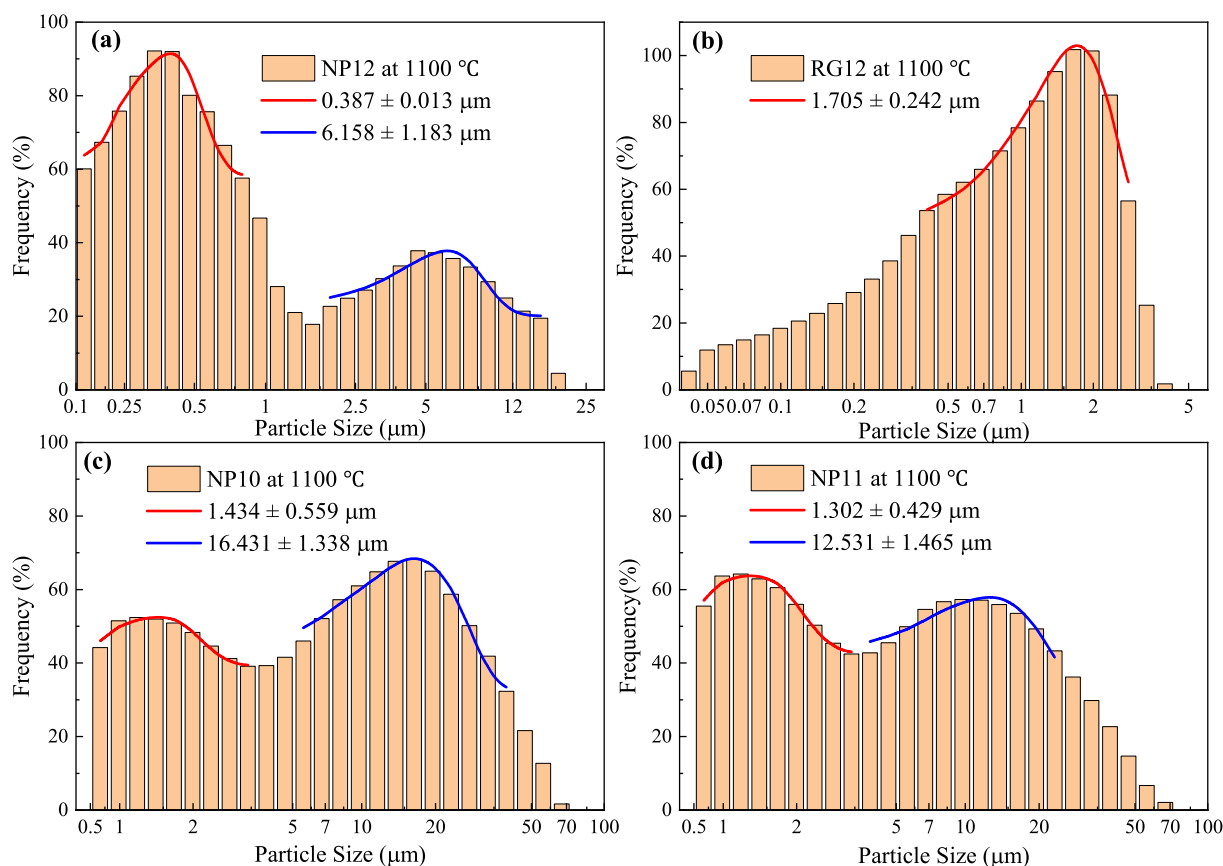


Fig. 5 Particle size distribution histograms of SrM powder: (a) NP12 sintered at 1100 °C; (b) RG12 sintered at 1100 °C; (c) NP10 sintered at 1100 °C; (d) NP11 sintered at 1100 °C. The red and blue lines are Gauss fit for smaller and larger particles.

of NP12 to be too large and this decreased the H_{cJ} . It has been reported that higher H_{cJ} can be obtained if SrM is sintered from nanocrystalline powders compared to the material derived from bulk powders (Guzman-Minguez et al., 2021; Holscher et al., 2020). The increased H_{cJ} of NP12 sintered at 1100 °C was mainly due to the presence of relatively smaller grains, which accounted for 70 %, in the compact sintered from the nano-sized Fe₃O₄ particles. Such high H_{cJ} (348.9 kA/m) of randomly oriented SrM is an improvement compared with other iron resources in solid-state method, as Table 1 shows.

The room temperature hysteresis loops of NP12 and RG12 sintered at 1100 °C can be seen from Fig. 6(b). RG12 with H_{cJ} being 259 kA/m and M_S being 52.3 emu/g had worse magnetic properties compared to NP12. This clearly shows that the different morphologies of Fe₃O₄ have a sensitive influence on the structure and properties of SrM. Moreover, the maximum magnetic product $(BH)_{max}$ is also an important parameter for permanent magnets (Saura-Muzquiz et al., 2018), and the calculated $(BH)_{max}$ of NP12 and RG12 are 1.521 and 1.018 MGOe, respectively. Obviously, using Fe₃O₄ NPs has advantages for higher $(BH)_{max}$.

Fig. 6(c) reveals the influence of the Fe/Sr atom ratio on the hysteresis loops of NP12, NP11 and NP10 sintered at 1100 °C. As mentioned in Section 3.2, the nano/micron ratio of the self-composition of these three specimens showed that H_{cJ} enhanced with an increase in Fe/Sr ratio, due to contribution from the single domain nano-sized grains (Gu et al., 2013).

But the M_S of NP12, NP11 and NP10 showed a different trend, because in NP10 there was no unreacted α -Fe₂O₃ at 1100 °C and good plate-like grains as shown in Fig. 3(e), which is contributed to M_S (Kubo et al., 1985). While NP11 had α -Fe₂O₃ and the particles were mostly spherical, which seems detrimental to M_S . It can be seen from Fig. 1(b) that NP12 had the best crystallinity, resulting in a higher M_S . The different tendency of H_{cJ} and M_S indicates the ratio of nano- and micron-particles is a crucial factor affecting magnetic properties. The self-composite material with 50 w.t.% nano- and 50 w.t.% micron-particles have been observed to make the H_{cJ} decrease instead (Shashanka et al., 2019). The number of our samples is too small to see the tendency of magnetic properties with Fe/Sr ratio, but from above results, the Fe/Sr ratio of 12 seems to be the most suitable in this preparation method. Moreover, the magnetocrystalline anisotropy K_1 of our samples can be determined from magnetic hysteresis loops by applying the law of approach to saturation (LATS) (Fabian, 2006). The obtained K_1 of NP12, NP11, NP10 and RG12 are 1.45, 1.38, 1.14 and 0.97×10^5 J/m³, respectively, and the value of NP12 is comparable with reported in literature (Dagar et al., 2020). It can also be seen that the high H_{cJ} is originated from the high K_1 .

The magnetic properties of the studied SrM were compared in detail with those reported recently using different Fe sources by solid-state method (Table 1). The comprehensive magnetic properties reported in other works are not as good as this work, especially the enhancement of H_{cJ} without losing M_S which is beneficial to practical applications as permanent

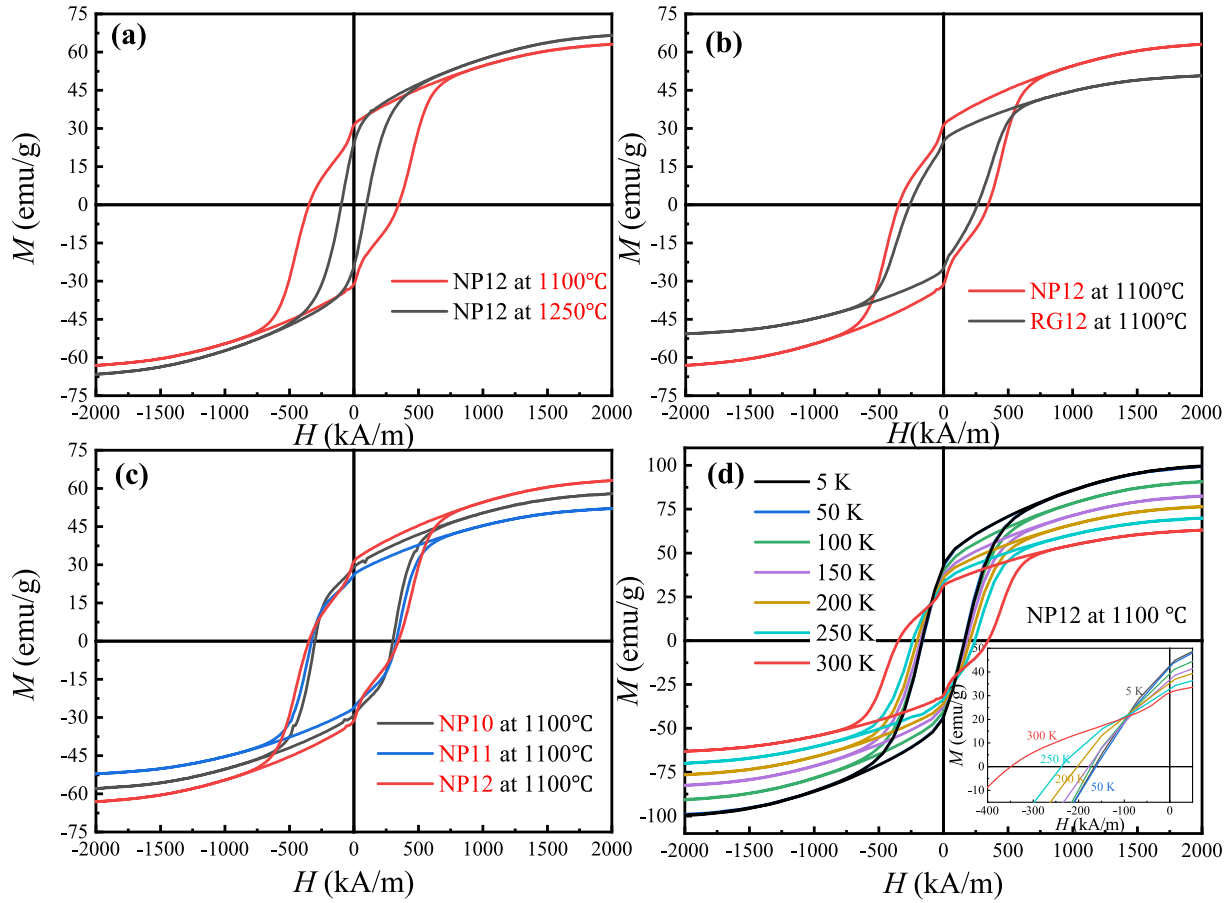


Fig. 6 The room temperature M – H hysteresis loops of: (a) NP12 sintered at 1100 °C and 1250 °C; (b) NP12 and RG12 sintered at 1100 °C; (c) NP10, NP11 and NP12 sintered at 1100 °C. And (d) temperature dependence of hysteresis loops, with the inset of enlargement of the second quadrant.

Table 1 The magnetic properties of M-type hexaferrite samples prepared by different iron source in the solid-state method.

Fe sources	Atom ratio of Fe/Sr	Sintering temperature (°C)	M_S (emu/g)	H_{cJ} (kA/m)	Ref.
Reagent Fe_2O_3	12	1000	~70	286	(Pullar, 2012)
Reagent Fe_2O_3	12	1100	48.4	235.5	(Li et al., 2020)
Spindle-like α - Fe_2O_3	11.5	1000	61.1	228.3	
Acicular α - $FeOOH$	11	1200	76.7	86.0	(Sun et al., 2018)
		1250	73.2	99.7	
Cubic-like α - Fe_2O_3	11	1200	62.2	195.9	(Xia et al., 2019)
		1250	63.1	167.8	
		1300	66.4	12.4	
Spindle-like α - Fe_2O_3	11	1200	53.4	143.2	
		1250	58.9	139.2	
		1300	62.3	116.8	
Fe_3O_4 NPs	10	1100	60.2	301.0	This work
	11	1100	54.3	328.3	
	12	1100	65.8	348.9	
		1250	69.5	97.8	
Reagent Fe_3O_4	12	1100	52.3	259.4	

magnets. High-quality iron sources can improve the purity of the product and enhance the M_S , but the high H_{cJ} is difficult to obtain. In this work, the high H_{cJ} of SrM was attributed to the realization of self-composition with 70 % nanocrystalline and 30 % micron-sized particles by using Fe_3O_4 NPs as iron resource.

It is worth noting that the hysteresis loop of NP12 at 1100 °C shows significant “kinks” in the second and fourth quadrants, generally occurring when the hard and soft magnetic phases are uncoupled or weakly coupled (Viet Nga and Lan, 2020). So, we wonder whether there is still unreacted soft magnetic Fe_3O_4 or oxidized γ - Fe_2O_3 in this case, although

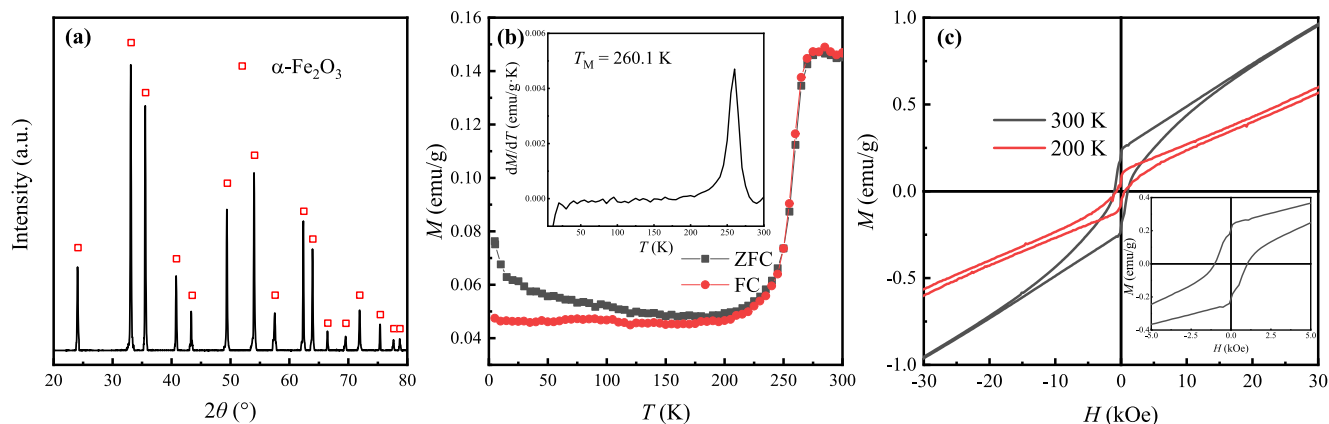


Fig. 7 The phase and magnetic properties of the product after sintering at 1100 °C from individual Fe_3O_4 NPs: (a) the XRD pattern; (b) ZFC and FC curves under an external field of 100 Oe, with the inset of differential of the ZFC curve; (c) $M-H$ curves at 200 and 300 K with the inset of an enlarge of the curve at 300 K at low field.

these two phases are almost impossible to exist at a high temperature like 1100 °C (Feitknecht and Gallagher, 1970). In order to distinguish whether the “kinks” in the hysteresis loop are caused by the exchange coupling between the two phases in nanocomposite or by the single-phase magnet, the hysteresis loops of NP12 at low temperature were measured. Generally, the increased anisotropy of hard phase and reduced length of the exchange coupling result in decoupling at low temperature, causing two magnetization reversals in the hysteresis loops (Kneller and Hawig, 1991). However, it can be seen from Fig. 6(d) that the hysteresis loops at low temperature are smooth, indicating that there were no soft magnetic phases in NP12 at 1100 °C.

For further verify the single hard magnetic phase of NP12, we sintered Fe_3O_4 NPs individually to 1100 °C with the same heating procedure. Because the X-ray diffraction peaks of Fe_3O_4 and $\gamma\text{-Fe}_2\text{O}_3$ are the same, but almost overlap with that of $\text{SrFe}_{12}\text{O}_{19}$ and cannot be easily distinguished. We analyzed the phase and magnetic properties of the obtained product, displayed in Fig. 7. As shown in Fig. 7(a), only $\alpha\text{-Fe}_2\text{O}_3$ was detected in the XRD measurement, indicating that Fe_3O_4 NPs were completely oxidized at 1100 °C. Then ZFC-FC curves were measured as shown in Fig. 7(b) and the ZFC was differentiated (see in the inset of Fig. 7(b)) to obtain the Morin phase transition temperature. The peak of the differential curve corresponds to the Morin phase transition temperature of 260.1 K, which was slightly lower than the reported 263 K (Morin, 1950). It has been reported that the Morin phase transition temperature will decrease with decreasing particle size (Amin and Araj, 1987). To verify the weak ferromagnetism above the Morin phase transition temperature and the antiferromagnetism below it, the hysteresis loops of the samples at 200 and 300 K were measured. As shown in Fig. 7(c), the $M-H$ curve at 200 K was almost a straight line, and there was almost no hysteresis at low field, indicating that the antiferromagnetism of the sample below the Morin phase transition; while the $M-H$ curve at 300 K exhibits obvious ferromagnetism in the low field with a magnetic moment of 0.18 emu/g and a coercivity of 1 kOe. All the results show that Fe_3O_4 NPs are completely oxidized to $\alpha\text{-Fe}_2\text{O}_3$ without Fe_3O_4 or $\gamma\text{-Fe}_2\text{O}_3$, further indicating that the “kinks” are not caused by the composite phase. It is because the weak ferromagnetism

of $\alpha\text{-Fe}_2\text{O}_3$ at 300 K, the “kinks” on the hysteresis loop of NP12 at room temperature are likely to be interfered with by residual $\alpha\text{-Fe}_2\text{O}_3$, while $\alpha\text{-Fe}_2\text{O}_3$ shows antiferromagnetism at low temperature, so the hysteresis loops of NP12 become smooth at low temperature.

The results discussed above show, firstly that the SrM ferrite prepared by the simple solid-state reaction using Fe_3O_4 NPs as iron source exhibit increased coercivity of 348.9 kA/m due to a unique formation mechanism, which is also the mechanism of improved magnetic properties by mechanical ball-milling. Since the process of using Fe_3O_4 NPs to form nano- and micron- composites is shorter than that of self-composite method, we commend the method in this work as the idea of high-performance magnets, and the related microstructure of SrM ferrite deserves further research, such as combining with the molten salt method. Although “kinks” appear in the hysteresis loop at room temperature due to the weak ferromagnetism of unreacted $\alpha\text{-Fe}_2\text{O}_3$, the $(BH)_{\text{max}}$ exhibits to be 1.521 MGOe, which doesn’t affect it at all as a possible material for magnetic recording, data storage, etc.

4. Conclusions

$\text{SrFe}_{12}\text{O}_{19}$ samples were prepared by solid-state method with Fe_3O_4 NPs as iron resource. Comparing different iron resources, sintering temperature and Fe/Sr atom ratios, the sample with the optimum H_{cJ} of 348.9 kA/m was obtained, which was an improvement compared to SrM obtained by other iron resources in solid-state method. Through the study of its microstructure and magnetic properties, it was found that the SrM, sintered at 1100 °C from Fe_3O_4 NPs with Fe/Sr atom ratio of 12, enabled the regulation of the microstructure by self-composite with 70 % nanocrystalline and 30 % micron-sized particles. Different formation mechanisms cause the variety of magnetic properties, which had been rarely studied. This work provides a new idea for the research of high-performance ferrite permanent materials.

CRediT authorship contribution statement

Ruoshui Liu: Conceptualization, Methodology, Investigation, Writing – original draft. **Di’an Wu:** Investigation, Data curation. **Xiang Yu:** Formal analysis, Writing – review & editing. **Ningfang Zhou:** Data curation. **Dan Liu:** Writing – review &

editing. **Lichen Wang:** Writing – review & editing. **Zhiyi Xu:** Writing – review & editing. **Huayang Gong:** Supervision. **Tongyun Zhao:** Supervision. **Jirong Sun:** Resources. **Fengxia Hu:** Resources. **Baogen Shen:** Resources, Supervision.

Declaration of Competing Interest

The authors declare that they have no known competing financial interests or personal relationships that could have appeared to influence the work reported in this paper.

Acknowledgements

This work was supported by the Science Center of the National Science Foundation of China (52088101), the National Key Research and Development Program of China (2021YFB3501202, 2020YFA0711502, 2019YFA0704900, 2018YFA0305704), the National Natural Sciences Foundation of China (U1832219, 51971240, 52101228, 52001012), the Strategic Priority Research Program B (XDB33030200), Beijing Natural Science Foundation (2214070) and the key program of the Chinese Academy of Sciences (ZDRW-CN-2021-3).

References

- Amin, N., Arais, S., 1987. Morin temperature of annealed submicronic α -Fe₂O₃ particles. *Phys. Rev. B* 35, 4810.
- Anantharamaiah, P.N., Joy, P.A., 2019. Large enhancement in the magnetostriction parameters of the composite of CoFe₂O₄ and CoFe_{1.9}Ga_{0.1}O₄. *Mater. Lett.* 236, 303–306. <https://doi.org/10.1016/j.matlet.2018.10.115>.
- Ashiq, M.N., Shakoor, S., Najam-ul-Haq, M., Warsi, M.F., Ali, I., Shakir, I., 2015. Structural, electrical, dielectric and magnetic properties of Gd-Sn substituted Sr-hexaferrite synthesized by sol-gel combustion method. *J. Magn. Magn. Mater.* 374, 173–178. <https://doi.org/10.1016/j.jmmm.2014.08.020>.
- Dagar, S., Hooda, A., Khasa, S., 2020. Structural and magnetic investigations of innovative lead-free particulate composites of NBT- M-Type SrFe₁₂O₁₉ Hexaferrite. *Vacuum* 177. <https://doi.org/10.1016/j.vacuum.2020.109436>.
- Fabian, K., 2006. Approach to saturation analysis of hysteresis measurements in rock magnetism and evidence for stress dominated magnetic anisotropy in young mid-ocean ridge basalt. *Phys. Earth Planet. Inter.* 154, 299–307. <https://doi.org/10.1016/j.pepi.2005.06.016>.
- Feitknecht, W., Gallagher, K.J., 1970. Mechanisms for the oxidation of Fe₃O₄. *Nature* 228, 548–549. <https://doi.org/10.1038/228548a0>.
- Fu, Y.P., Lin, C.H., 2005. Fe/Sr ratio effect on magnetic properties of strontium ferrite powders synthesized microwave-induced combustion process. *J. Alloys Compd.* 386, 222–227. <https://doi.org/10.1016/j.jallcom.2004.04.148>.
- Granados-Mirallas, C., Jenuš, P., 2021. On the potential of hard ferrite ceramics for permanent magnet technology—a review on sintering strategies. *J. Phys. D Appl. Phys.* 54. <https://doi.org/10.1088/1361-6463/abfad4>.
- Gu, F.M., Pan, W.W., Liu, Q.F., Wang, J.B., 2013. Electrospun magnetic SrFe₁₂O₁₉ nanofibres with improved hard magnetism. *J. Phys. D Appl. Phys.* 46, 445003. <https://doi.org/10.1088/0022-3727/46/44/445003>.
- Guzman-Minguez, J.C., Moreno-Arche, L., Granados-Mirallas, C., Lopez-Sanchez, J., Marin, P., Fernandez, J.F., Quesada, A., 2021. Boosting the coercivity of SrFe₁₂O₁₉ nanocrystalline powders obtained using the citrate combustion synthesis method. *J. Phys. D Appl. Phys.* 54. <https://doi.org/10.1088/1361-6463/abb846>.
- Holscher, J., Saura-Muzquiz, M., Ahlburg, J., Morch, M., Gronseth, D.K., Christensen, M., 2020. Controlling structural and magnetic properties of SrFe₁₂O₁₉ nanoplatelets by synthesis route and calcination time. *J. Phys. D Appl. Phys.* 53. <https://doi.org/10.1088/1361-6463/abaae1>.
- Jean, M., Nachbaur, V., Bran, J., Le Breton, J.M., 2010. Synthesis and characterization of SrFe₁₂O₁₉ powder obtained by hydrothermal process. *J. Alloys Compd.* 496, 306–312. <https://doi.org/10.1016/j.jallcom.2010.02.002>.
- Kaczmarek, W.A., Idzikowski, B., Müller, K.H., 1998. XRD and VSM study of ball-milled SrFe₁₂O₁₉ powder. *J. Magn. Magn. Mater.* 177–181, 921–922. [https://doi.org/10.1016/s0304-8853\(97\)00839-1](https://doi.org/10.1016/s0304-8853(97)00839-1).
- Katlakunta, S., Meena, S.S., Srinath, S., Bououdina, M., Sandhya, R., Praveena, K., 2015. Improved magnetic properties of Cr³⁺ doped SrFe₁₂O₁₉ synthesized via microwave hydrothermal route. *Mater. Res. Bull.* 63, 58–66. <https://doi.org/10.1016/j.materresbull.2014.11.043>.
- Kim, S.-D., Kim, J.-S., 2006. Magnetic properties of Sr-ferrites synthesized in molten (NaCl + KCl) flux. *J. Magn. Magn. Mater.* 307, 295–300. <https://doi.org/10.1016/j.jmmm.2006.04.019>.
- Kneller, E.F., Hawig, R., 1991. The exchange-spring magnet: a new material principle for permanent magnets. *IEEE Trans. Magn.* 27, 3588–3596.
- Kubo, O., Ido, T., Yokoyama, H., Koike, Y., 1985. Particle size effects on magnetic properties of BaFe₁₂–2xTixCoxO₁₉ fine particles. *J. Appl. Phys.* 57, 4280–4282. <https://doi.org/10.1063/1.334585>.
- Li, X., Yang, W., Bao, D., Meng, X., Lou, B., 2013. Influence of Ca substitution on the microstructure and magnetic properties of SrLaCo ferrite. *J. Magn. Magn. Mater.* 329, 1–5. <https://doi.org/10.1016/j.jmmm.2012.10.004>.
- Li, H., Yi, X., Wu, Y., Wei, X., Deng, D., Zheng, L., Luo, W., Luo, X., Gong, R., Zhang, M., 2020. Molten salt synthesis, formation mechanism and greatly enhanced magnetic properties of randomly oriented BaM ferrite. *J. Alloys Compd.* 827. <https://doi.org/10.1016/j.jallcom.2020.154083>.
- Liu, Q., Wu, C.S., Wang, Y., Zhou, L., Li, J., Liu, Y.L., Zhang, H.W., 2019. Textured M-type barium hexaferrite Ba(ZnSn)_xFe₁₂-2xO₁₉ with c-axis anisotropy and high squareness ratio. *Ceram. Int.* 45, 4535–4539. <https://doi.org/10.1016/j.ceramint.2018.11.138>.
- Masoudpanah, S.M., Ebrahimi, S.A.S., 2011. Fe/Sr ratio and calcination temperature effects on processing of nanostructured strontium hexaferrite thin films by a sol-gel method. *Res. Chem. Intermed.* 37, 259–266. <https://doi.org/10.1007/s11164-011-0286-y>.
- Mohaideen, K.K., Joy, P.A., 2012. Enhancement in the magnetostriction of sintered cobalt ferrite by making self-composites from nanocrystalline and bulk powders. *ACS Appl. Mater. Interfaces* 4, 6421–6425. <https://doi.org/10.1021/am302053q>.
- Morin, F.J., 1950. Magnetic susceptibility of α -Fe₂O₃ and α -Fe₂O₃ with added titanium. *Phys. Rev.* 78, 819–820. <https://doi.org/10.1103/PhysRev.78.819.2>.
- Oh, N., Park, S., Kim, Y., Kwon, H., Kim, S., Lim, K., 2020. Magnetic properties of M-type strontium ferrites with different heat treatment conditions. *Rare Met.* 39, 84–88. <https://doi.org/10.1007/s12598-019-01251-0>.
- Pullar, R.C., 2012. Hexagonal ferrites: A review of the synthesis, properties and applications of hexaferrite ceramics. *Prog. Mater. Sci.* 57, 1191–1334. <https://doi.org/10.1016/j.pmatsci.2012.04.001>.
- Pullar, R.C., Bdkin, I.K., Bhattacharya, A.K., 2012. Magnetic properties of randomly oriented BaM, SrM, Co₂Y, Co₂(Z) and Co₂W hexagonal ferrite fibres. *J. Eur. Ceram. Soc.* 32, 905–913. <https://doi.org/10.1016/j.jeurceramsoc.2011.10.047>.
- Remya, K.P., Prabhu, D., Amirthapandian, S., Viswanathan, C., Ponpandian, N., 2016. Exchange spring magnetic behavior in BaFe₁₂O₁₉/Fe₃O₄ nanocomposites. *J. Magn. Magn. Mater.* 406, 233–238. <https://doi.org/10.1016/j.jmmm.2016.01.024>.
- Sánchez-De Jesús, F., Bolarín-Miró, A., Cortes-Escobedo, C.A., Valenzuela, R., Ammar, S., 2014. Mechanosynthesis, crystal

- structure and magnetic characterization of M-type SrFe₁₂O₁₉. *Ceram. Int.* 40, 4033–4038.
- Sapoletova, N.A., Kushnir, S.E., Li, Y.H., An, S.Y., Seo, J.-W., Hur, K.H., 2015. Plate-like SrFe₁₂O₁₉ particles prepared by modified sol–gel method. *J. Magn. Magn. Mater.* 389, 101–105. <https://doi.org/10.1016/j.jmmm.2015.04.055>.
- Saura-Muzquiz, M., Granados-Miralles, C., Andersen, H.L., Stin-gaciu, M., Avdeev, M., Christensen, M., 2018. Nanoengineered high-performance hexaferrite magnets by morphology-induced alignment of tailored nanoplatelets. *ACS Appl. Nano Mater.* 1, 6938–6949. <https://doi.org/10.1021/acsanm.8b01748>.
- Shashanka, H.M., Anantharamaiah, P.N., Joy, P.A., 2019. Magnetic parameters of SrFe₁₂O₁₉ sintered from a mixture of nanocrystalline and micron-sized powders. *Ceram. Int.* 45, 13592–13596. <https://doi.org/10.1016/j.ceramint.2019.04.023>.
- Shen, S.-Y., Zheng, H., Zheng, P., Wu, Q., Deng, J.-X., Ying, Z.-H., Zheng, L., 2021. Microstructure, magnetic properties of hexagonal barium ferrite powder based on calcination temperature and holding time. *Rare Met.* 40, 981–986. <https://doi.org/10.1007/s12598-018-1153-4>.
- Singh, J., Singh, C., Kaur, D., Zaki, H., Abdel-Latif, I.A., Narang, S. B., Jotania, R., Mishra, S.R., Joshi, R., Dhruv, P., Ghimire, M., Shirsath, S.E., Meena, S.S., 2017. Elucidation of phase evolution, microstructural, Mossbauer and magnetic properties of Co²⁺-Al³⁺ doped M-type Ba-Sr hexaferrites synthesized by a ceramic method. *J. Alloys Compd.* 695, 1112–1121. <https://doi.org/10.1016/j.jallcom.2016.10.237>.
- Sozeri, H., Baykal, A., Unal, B., 2012. Low-temperature synthesis of single-domain Sr-hexaferrite particles by solid-state reaction route. *Physica Status Solidi A-Appl. Mater. Sci.* 209, 2002–2013. <https://doi.org/10.1002/pssa.201228023>.
- Sun, R., Li, X., Xia, A., Su, S., Jin, C., 2018. Hexagonal SrFe₁₂O₁₉ ferrite with high saturation magnetization. *Ceram. Int.* 44, 13551–13555. <https://doi.org/10.1016/j.ceramint.2018.04.187>.
- Teja, A.S., Koh, P.-Y., 2009. Synthesis, properties, and applications of magnetic iron oxide nanoparticles. *Prog. Cryst. Growth Charact. Mater.* 55, 22–45. <https://doi.org/10.1016/j.pcrysgrow.2008.08.003>.
- Viet Nga, T.T., Lan, N.T., 2020. Fabrication and exchange-spring properties of SrFe₁₂O₁₉@Fe₃O₄ nanocomposites with core-shell structure. *Mater. Chem. Phys.* 251. <https://doi.org/10.1016/j.matchemphys.2020.123084>.
- Vijayalakshmi, A., Gajbhiye, N.S., 1998. Magnetic properties of single-domain SrFe₁₂O₁₉ particles synthesized by citrate precursor technique. *J. Appl. Phys.* 83, 400–406. <https://doi.org/10.1063/1.366654>.
- Wohlfarth, E.P., 1983. Magnetic properties of single domain ferro-magnetic particles. *J. Magn. Magn. Mater.* 39, 39–44. [https://doi.org/10.1016/0304-8853\(83\)90393-1](https://doi.org/10.1016/0304-8853(83)90393-1).
- Wu, L., Jubert, P.-O., Berman, D., Imano, W., Nelson, A., Zhu, H., Zhang, S., Sun, S., 2014. Monolayer assembly of ferrimagnetic Co_xFe_{3-x}O₄ nanocubes for magnetic recording. *Nano Lett.* 14, 3395–3399.
- Xia, A., Zhan, T., Sun, R., Su, S., Li, J., Zhang, H., Li, H., Jin, C., 2019. M-type SrFe₁₂O₁₉ ferrites obtained by using cubic or spindle-like α-Fe₂O₃ as Fe sources: a comparative study. *J. Alloys Compd.* 784, 276–281. <https://doi.org/10.1016/j.jallcom.2019.01.008>.
- Xu, L., Wang, H., Xu, Y., Wang, Q., Ma, X., Zhou, Z., Zou, Y., Xing, S., 2017. Formation mechanism of strontium hexaferrite compounds by complementary structure and thermogravimetry investigations. *Nanosci. Nanotechnol. Lett.* 9, 567–572. <https://doi.org/10.1166/nnl.2017.2358>.
- Zhu, D.-M., Geng, Z.-W., Liu, R.-M., Zhou, X.-W., Jia, L.-Y., Hu, G.-H., Wang, Q., Li, B.-S., 2020. Development of high-performance dry-pressed anisotropic permanent ferrite for La–Ca–Sr–Co system. *Rare Met.* 39, 89–94. <https://doi.org/10.1007/s12598-019-01260-z>.
- Zi, Z.F., Sun, Y.P., Zhu, X.B., Yang, Z.R., dai, J.M., Song, W.H., 2008. Structural and magnetic properties of SrFe₁₂O₁₉ hexaferrite synthesized by a modified chemical co-precipitation method. *J. Magnet. Magnet. Mater.* 320, 2746–2751. <https://doi.org/10.1016/j.jmmm.2008.06.009>.